OPTIMIZATION OF REACTOR TEMPERATURE ACCORDING TO RADIATION DISTRIBUTION CHARACTERISTICS

N. Ozalp[1*], M. Lipperheide[1], J. Sarwar[2]

[1]Katholieke Universiteit (KU) Leuven, Mechanical Engineering Department, 3000 Leuven, Belgium
[2]Texas A&M University at Qatar, Mechanical Engineering Department, P.O. Box 23874, Doha, Qatar

ABSTRACT

Temperature stability inside a solar reactor is much more complex to achieve than that of traditional combustion based reactors. The main reason contributes to the transient nature of the solar radiation which serves as the source of high temperature process heat to run endothermic solar thermochemical reactions. One of the key factors to assure temperature stability inside a solar reactor is to understand the characteristics of the incoming solar radiation and design a solar reactor accordingly. This paper provides radiation distribution characteristics of 7 kW high flux solar simulator and design of a solar reactor according to that heat source. Flux characterization of the solar simulator was done by using a calorimetric calibration of a heat flux gage. The maximum and minimum peak flux output at the focal plane was obtained by moving the heat flux gage within the focal plane, but away from the focal point by 0.25 mm steps. Heat exchange between the gage and the Lambertian target was quantified by measuring the inlet and outlet temperatures. Flux map obtained per experimental measurements was used to determine corresponding aperture size of the solar reactor for various flux levels. Selection of representative flux levels were made based upon NREL database which was fit to the flux scale of the 7 kW solar simulator. An optimum aperture size for the solar simulator was calculated for various corresponding time of the day per incoming flux based on two different optimization methods and input parameters in order to maintain a constant reactor temperature. It was found that the maximum optimal aperture radius during sunset at 5 am varies between 1.8 cm and 3.52 cm for the methods used, whereas it decreases to 0.4 cm and 0.73 cm during midday. Optimal constant reactor temperatures for corresponding aperture sizes change between 1339 K and 854 K per method used and flux distribution measured.

NOMENCLATURE

A	[m^2]	Absorbing surface area of the heat flux gage
$A_{Aperture}$	[m^2]	Aperture surface area
h_r	[W/m^2 K]	Radiative heat transfer coefficient
I	[kW/m^2]	Irradiance
L	[m]	Length of heat flux gage
$\dot{m}$	[kg/s]	Mass flow rate
q_g	[W]	Energy absorbed by the heat flux gage
q_l	[W]	Energy absorbed by the Lambertian target
q''_{sim}	[W/m^2]	Magnitude of the incident radiative flux
$R^*_{t,c}$	[m^2 K/W]	Interfacial thermal resistance
r_i	[m]	Distance of thermocouples from heat flux gage
T_g	[K]	Temperature of the gage
T_{target}	[K]	Average temperature of thermocouples
X	[-]	Dimensionless flux

Special characters

α	[-]	Absorptivity
ε	[-]	Emissivity
σ	[W/m^2 K^4]	Stefan-Boltzmann Constant neighbouring cooling inserts in the *y* direction

Subscripts

cond	Conduction
conv	Convection
eff	Volumetric effective expression
g	Gage
lamb	Lambertian
l	Lambertian
max	Maximum
sim	Absorbed radiative flux in gage
rerad	Reradiation

INTRODUCTION

Concentrated solar energy can provide high temperature process heat for electricity and fuel production. However, it is crucial to know the solar radiation intercepted by the aperture. Therefore, experimental measurement of the incident concentrated sunlight is necessary to quantify the amount of energy received by the reactor through the aperture. Reactor performance is highly dependent on incoming direct solar radiation. Throughout the day, the solar zenith angle changes leading to different flux levels and thus transient operation conditions within the reactor. This is an essential parameter taken into account for efficient reactor design that is minimally affected by the transient nature of the sun. From the heat transfer point of view, the main design constrain of a solar reactor design is the aperture radius [1]. An aperture radius can be optimized for different radiative flux levels at different solar zenith angles, thus different times of the day [2].

Incident flux measurement can be performed by several methods like by using a heat flux gage only [3], visualization using a spectrum-neutral pyrometer [4], or cylindrically masked photodiode [5], but most widely used technique is flux mapping method [6-13]. Utilization of flux mapping method requires calibration of the heat flux gage. The operating principle of heat flux gage is that it measures a voltage corresponding to the temperature difference between the center and the circumference of a thin circular foil disk of the heat flux gage. The measured output voltage relates direct proportionally to the heat flux via the Seeback effect.

*Corresponding Author: nesrin.ozalp@kuleuven.be

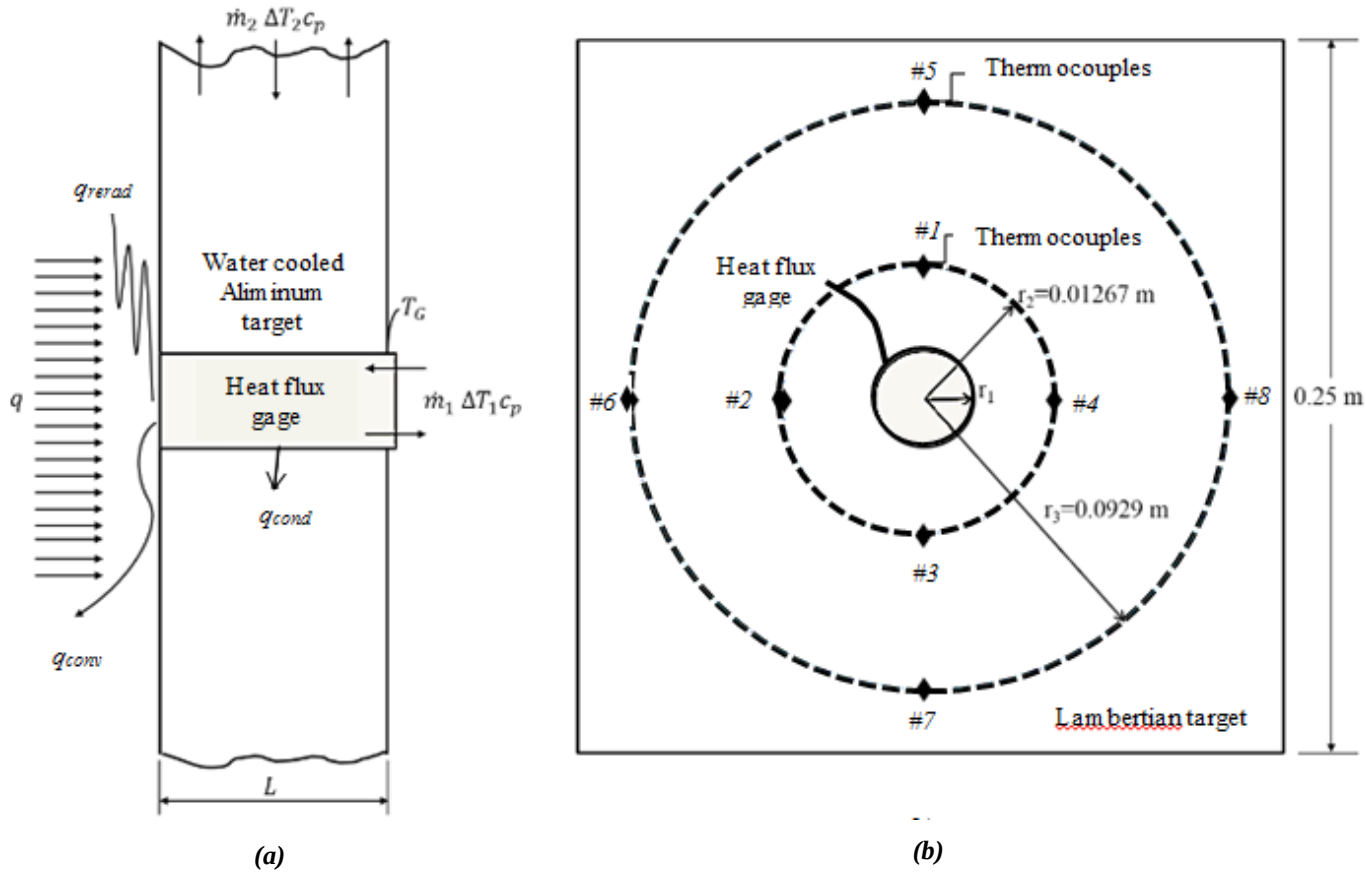

Figure 1 Schematic illustration of calorimetric calibration method per (a) side view, and (b) front view of the target

There are several methods to calibrate heat flux gage. For example, the heat flux gage is plunged quickly in the furnace after it is brought and stabilized to the temperature representing the heat flux level with a low flow of argon. The output is recorded continuously using pyrometer until heat flux begins to decrease. Then Stefan-Boltzmann equation is used to calculate the heat flux using measured temperatures of the furnace and the transducer [14]. This method does not consider the difference between emission spectrum from the heat source in the furnace and spectral absorptivity of the heat flux gage which may results in an over prediction of the heat flux. The other calibration procedure is based on the thermal balance [15]. The experimental setup consists of the heat flux gage placed in stainless steel housing. All the surfaces of the gage and housing are insulated with low-conductivity insulation except the entire front face of the gage. Temperatures of the insulation are measured using thermocouples and a differential thermocouple measures the temperature increment between water inlet and outlet port. The sensor was used as a calorimeter and calibration factor was obtained. Thermal and convective losses/gains on the front face of the sensor due to change in cooling conditions; ambient temperature or incident heat flux were ignored. Another calorimetric calibration method is being used by Krueger et al. (2012) to relate output of a heat flux gage with the greyscale value of a CCD camera [12]. The experimental setup consists of a water-cooled heat flux gage placed in a Lambertian target. A thermocouple attached at the back of the heat flux gage measure its temperature while four attached thermocouples at the Lambertian target measure its temperature. The energy transferred by conduction between the gage and the Lambertian target coupled with the energy transferred to the cooling water calculates heat flux at the gage using energy balance equation. This method considers incident heat flux only on the heat flux gage and ignores effect of re-radiation losses from the gage and Lambertian target.

For lab-scale experiments, transient behaviour of the sun can be produced using a solar simulator by adjusting the power consumption which in turn changes the flux levels intercepted by the reactor. In this paper, radiation distribution of a high flux solar simulator is characterized based on the calorimetric calibration method. This method includes the heat flux incident on the Lambertian target as well as on the heat flux gage. Conduction and re-radiation losses from the Lambertian target are also considered and the flux distribution over the surface area is calculated. The paper also elaborates a method to optimize aperture size per flux distribution of the solar simulator obtained via heat flux gage experiments.

METHODOLOGY

Figure 1 shows a schematic illustration of the calorimetric calibration method with the heat gage placed on Lambertian target. Incoming solar radiation q can be calculated as follows:

$$q = \dot{m}\,\Delta T_1 c_p + q_{cond} + q_{conv} + q_{rerad} + \dot{m}\Delta T_2 c_p \quad (1)$$

Where '$\dot{m}$' is the mass flow rate of the cooling water circulating through the heat flux gage, c_p is the specific heat capacity of water and ΔT_1 is the temperature difference measured using thermocouples located at the inlet and exit of the cooling water streams from heat flux gage. Temperature difference measured using thermocouples located at the inlet and outlet port of water from Lambertian target is referred as ΔT_2. As for q_{cond}, it is the conduction heat transfer between the gage and the encapsulating Lambartian target. q_{conv} is the heat lost by convection at the boundary and q_{rerad} is reradiated heat flux. Heat lost by convection can be ignored as it accounts for 0.1% for the setup shown in Figure 1 [12]. The part of the energy incident on the selected system is transferred to heat flux gage while rest is transferred to Lambertian target. Therefore, energy incident on the system 'q' can be written as:

$$q = q_g + q_l \quad (2)$$

Where q_g is the energy absorbed by the heat flux gage while q_l is the energy absorbed by the Lambertian target. The magnitude of the incident radiative flux q''_{sim} over the heat flux gage can be measured using a calorimetric calibration method. The magnitude of incident radiative flux 'q''_{sim}' relates to the energy absorbed by the heat flux gage q_g as follows [12]:

$$q''_{sim} = \frac{q_g}{A\,\alpha} \quad (3)$$

Here *A* is the absorbing surface area of the heat flux gage and α is the total hemispherical absorptivity of the gage coating. The energy transferred to the Lambertian target calculates:

$$q_l = q_{cond\ lamb} + q_{conv\ lamb} + q_{rerad\ lamb} + \dot{m}\Delta T_2 c_p \quad (4)$$

Conduction through the system 'q_{cond}' is calculated as:

$$q_{cond} = \frac{T_G - T_{target1}}{\frac{R^*_{t,c}}{2\pi r_1 L} + \frac{\ln\left(\frac{r_2}{r_1}\right)}{2\pi k L} + \frac{\ln\left(\frac{r_3}{r_2}\right)}{2\pi k L}} \quad (5)$$

Where 'r_1', 'r_2' and 'r_3' are the radii as shown in Figure 1, '*k*' is the conductivity of aluminium, 'T_G' is the temperature of the gage, 'T_{target}' is the average temperature of four thermocouples located at radius 'r_3' and 'L' is the length of the heat flux gage. '$R^*_{t,c}$' represents the contact resistance. The Equation 5 can be used to calculate the conduction heat transfer between heat flux gage and aluminium target at incident energy 'q'. Although contact resistance between heat flux gage and aluminium target can be found analytically [16-18], it is assumed to be 2.75×10^{-4} $m^2K\ W^{-1}$ for an aluminium interface with air as the interfacial fluid [12].

The conduction through the Lambertian target '$q_{cond\ lamb}$' due to incident energy 'q_l' at the Lambertian target calculates as:

$$q_{cond\ lamb} = \frac{T_{target1} - T_{target2}}{\frac{R^*_{t,c}}{2\pi(r_2 - r_1)L} + \frac{\ln\left(\frac{r_3}{r_2}\right)}{2\pi k L}} \quad (6)$$

Where '$T_{target2}$' is the average temperature of four thermocouples located at radius 'r_2'. Re-radiation from the selected surface calculates as:

$$q_{rerad} = h_r A_s \Delta T \text{ where } h_r = \sigma\varepsilon F \frac{T_s^4 - T_{target2}^4}{T_s - T_{target2}} \quad (7)$$

Where 'h_r' is the radiative heat transfer coefficient, 'A_s' represents the area of the selected surface with '*s*' denoting either heat flux gage or Lambertian target.

After calculating components of energy balance equation using Equations 4 to 7, the total energy incident on the system and on the Lambertian target can be found using equation 1 and 4 respectively. Then the energy incident on the heat flux gage can be obtained using Equation 2 and lastly, heat flux incident on the gage can be calculated using Equation 3.

EXPERIMENTAL SETUP

A high flux solar simulator, heat flux gage, Lambertian target, three axes movement controller (XYZ slider), LabVIEW (Laboratory Virtual Instrument Engineering Workbench) software, and National Instruments hardware for data acquisition make up the instrumentation used during experimentation. The experimental setup is shown below in Figure 2.

A similar experimental setup has been explained by authors' elsewhere for characterization of the solar simulator using a flux mapping method [19]. In this heat flux gage calibration experiment, the Lambertian target has a different configuration as shown in Figure 3 and variable flow was used for the cooling of the Lambertian target in order to include the effect of re-radiation losses and energy incident on both heat flux gage and Lambertian target. Nevertheless, experimental setup is explained here in detail for completeness for this heat flux gage calibration experiment. The high flux solar simulator utilizes an ozone free 7 kW xenon short-arc lamp [20], as the light source. The light is then directed at a 25cm x 25cm aluminium target which has been plasma-coated with Al_2O_3 to achieve near-Lambertian diffuse reflection and milled internally in order to allow water cooling [21]. The temperature of the Lambertian target was monitored at radii 'r_2' and 'r_3' as shown in Figure 1. Four K-type thermocouples were used at radius 'r_2' while four J-type thermocouples were used at radius

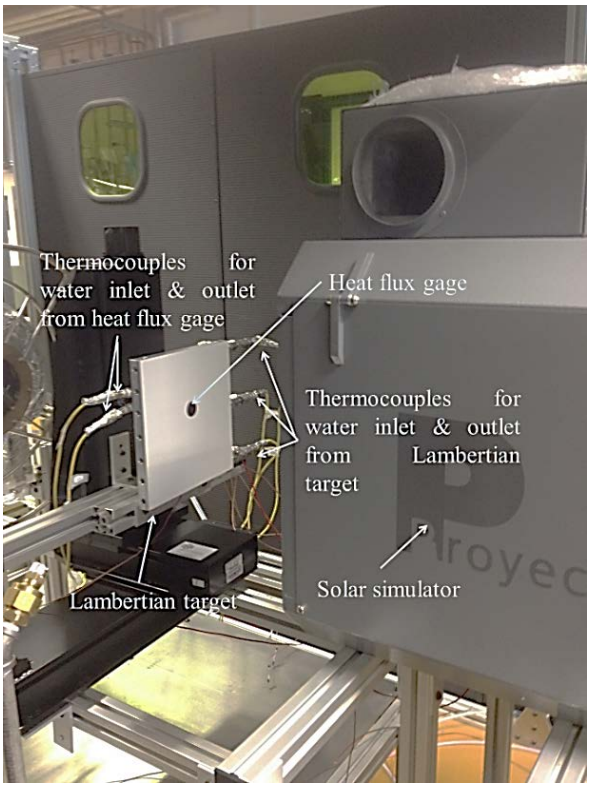

Figure 2 Experimental setup of heat flux gage calibration which shows the solar simulator, Gordon-type circular foil radiometer referred as heat flux gage inserted in Lambertian target to measure incident flux, water inlet and outlet ports (with thermocouples) to control temperature of Lambertian target and heat flux gage

'r_3' to prevent overheating and damage of plasma coating. A schematic of thermocouples locations is presented in Figure 3.

A compact real-time input/output (cRIO) module NI-9213 [22], received all thermocouple signals and data was recorded through LabVIEW. The heat flux gage output was detected by cRIO module NI-9211 [21]. The measurement sensitivity of NI-9211 and NI-9213 is 0.008 mV [23] (corresponding to 0.4 kWm^{-2}) and 0.02 $^{\circ}C$ [22], respectively. National Instruments module NI-9213 integrates cold-junction compensation, preliminary signal filtering, and amplification when converting analogue data from the thermocouples to 24-bit digital data. A local PC received the digital signals from the NI cRIO, displaying and recording the signals acquired.

The intensity of the incident flux was measured with a Gordon-type circular foil radiometer (Vatell TG1000-0) with colloidal graphite coating. This radiometer works as a differential thermocouple, measuring the temperature differential between the centre and the edge of heat flux gage. The radiometer outputs 1 mV for every 491.46 kWm^{-2} of incident flux with a sensitivity of 0.002 mV/kWm^{-2} [24]. The absorptivity of the colloidal graphite coating has been determined to be 0.8135 ± 0.0004 [12]. Cooling of the heat flux gage was achieved using a flow meter with a range of 3.15 × 10^{-5} m^3s^{-1} to 3.15 × 10^{-4} m^3s^{-1}. Flow was maintained constantly at 3.15 × 10^{-5} m^3s^{-1} in heat flux gage. The water flow in the Lambertian target was varied in the range of 6.25 × 10^{-5} m^3s^{-1} to 8.2 × 10^{-5} m^3s^{-1}.

Figure 2 shows the Lambertian target mounted on the XYZ slider in order to bring the experimental setup to the focal point

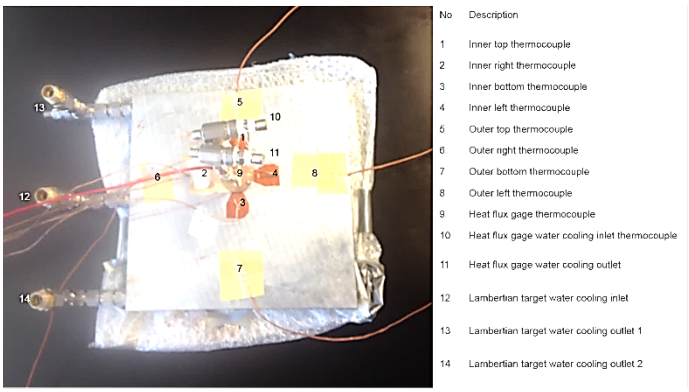

Figure 3 A schematic of all thermocouples locations on the system containing heat flux gage, Lambertian target and water inlet, outlet port

of the solar simulator and to change the flux conditions on the experimental setup. The XYZ slider consists of three precision slides with a resolution of 0.08 µm and 1 µm repeatability [25]: NLS8-500-101 slides for the x-axis movement, NLS8-300-102 slider for the y-axis movement and NLS8-200-101 slider for the z-axis movement. The motion controller (NSC-G3) performed independent and coordinated motion of sliders during experimentation [26].

Solar simulator was optically aligned first and then the Lambertian target was brought to the focal point. The heat flux gage was moved within the optical plane in the y-axis (as shown in Figure 2) for 7 cm in steps of 0.25 mm. Each measurement of temperature and heat flux gage output was recorded over an interval of 15 s and incident heat flux measurements were averaged in time. Experiments were repeated at various water flow rates to ensure independence of the experimental output on cooling water flow and therefore temperature.

RESULTS AND DISCUSSION

Experiments were performed at different flow rates and dynamic temperatures were recorded. Temperature readings at maximum flow rate of water (8.2 × 10^{-5} m^3s^{-1}) to Lambertian target over the time are shown in Figure 4 where the upper four curves represent the readings by thermocouples located at the inner circle of the Figure 1 (b), and the lower four curves represent the readings by thermocouples located at the outer circle of the Figure 1 (b). The highest heat flux gage temperature was found in the beginning due to its placement at the focal point of solar simulator. The flux was also incident on the Lambertian target which results in higher temperature at the inner thermocouples. The outer thermocouples were at the lower temperature as compared to inner thermocouples. The variation in the temperature at different locations of the system showed that heat flux incident on the system was not uniform.

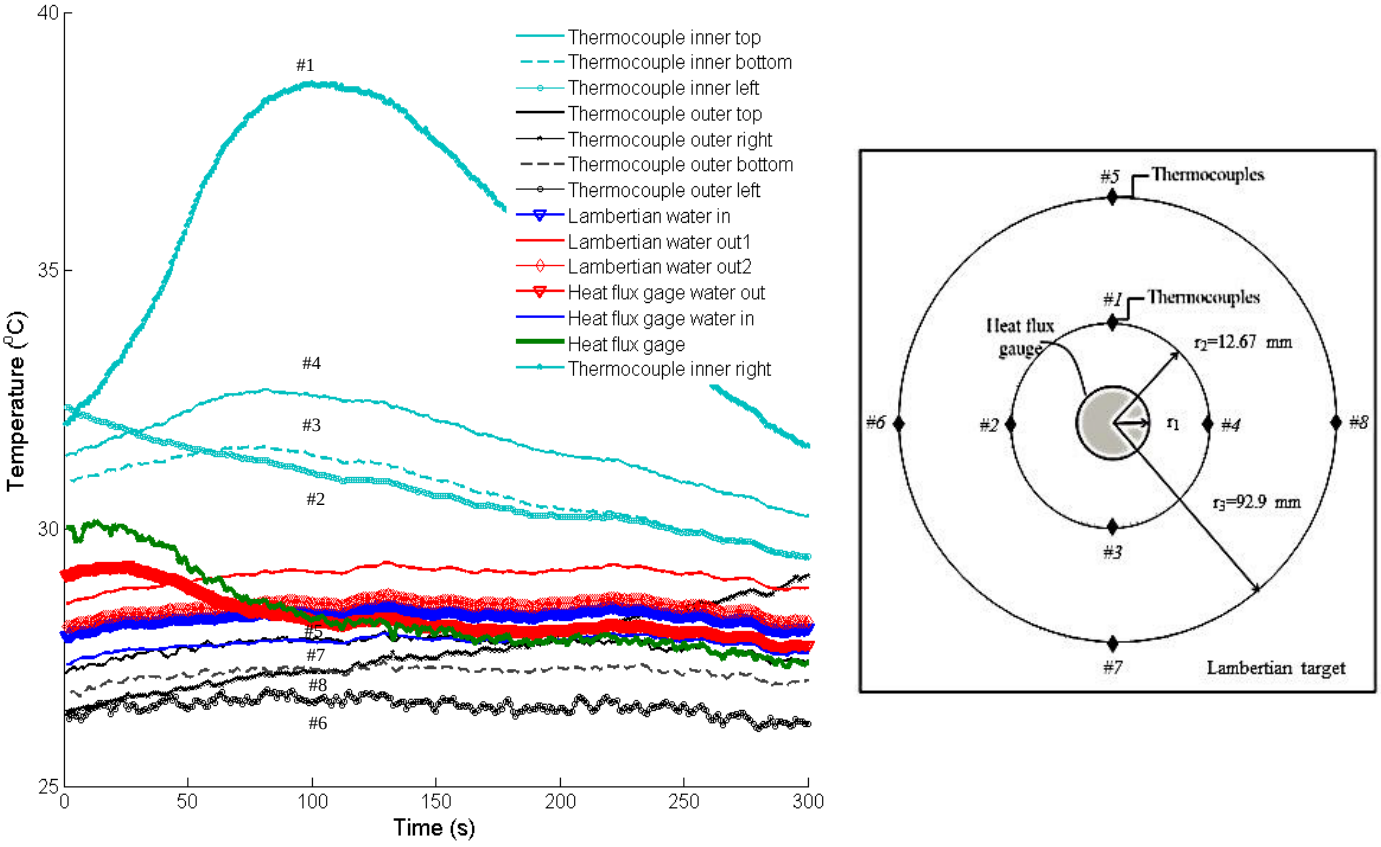

(a) *(b)*

Figure 4 *(a)* Temperature readings by thermocouples, *(b)* Location of the thermocouples

The calorimetric calibration method proposed in section 2 was used to calculate energy absorbed by the heat flux gage and by the Lambertian target. The result is given in Figure 5 which shows that the heat flux gage absorbs more energy when placed at the focal point as compared to Lambertian target. When heat flux gage starts moving away from the focal point, the energy absorption decreases and concomitantly, energy absorbed in Lambertian target increases. When heat flux gage is moved fully away from the focal point i.e. ~12 mm then Lambertian target receives more energy as compared to the heat flux gage. The energy absorbed by the Lambertian target continues to increase until heat flux gage is 30 mm away from the focal point. After 30 mm, the energy absorbed by Lambertian target gets steady before reducing after 40 mm.

The energy absorbed by the heat flux gage was used to quantify the incident heat flux using Equation 3. The comparison of energy absorbed by heat flux gage using proposed calorimetric calibration method and calibration factors available in literature was carried and the result is shown in Figure 6.

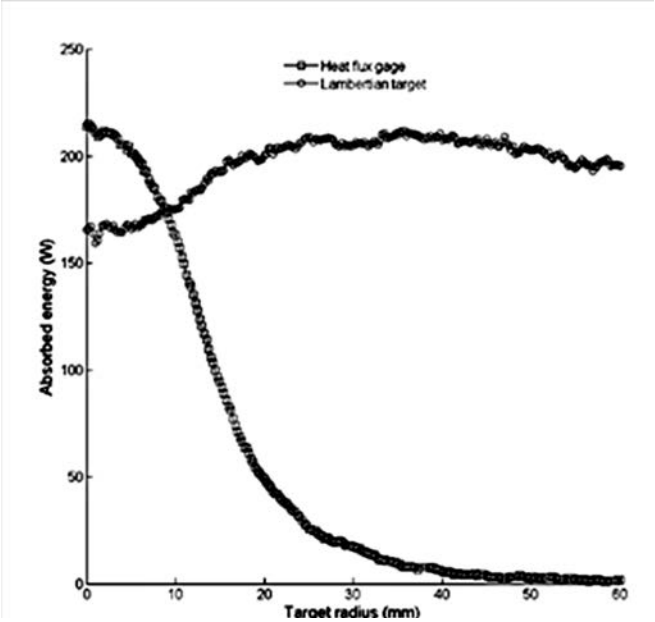

Figure 5 Energy absorbed by the heat flux gage and by the Lambertian target at varying target radii

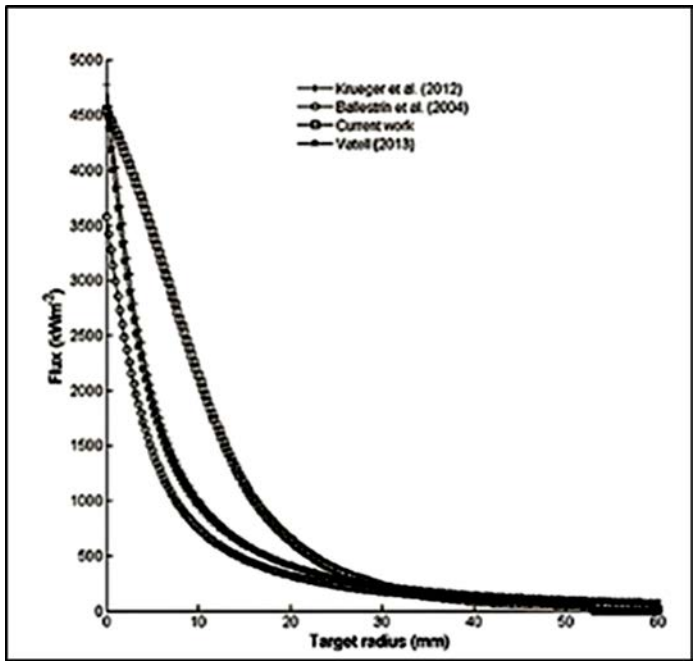

Figure 6 Comparison of obtained incident heat flux on the heat flux gage using proposed enhanced calorimetric calibration method and obtained heat flux using calibration factors proposed by manufacturer, Krueger et al. (2012) and Ballestrin et al. (2004) [12, 15]

Figure 6 gives the distribution trend of the incident heat flux on the heat flux gage. It is seen that the results obtained from enhanced calibration method shows good agreement with distributions calculated by using calibration factor available in literature. The heat flux calculated using proposed method at the focal point is in good agreement with the heat flux calculated using manufacturer's calibration factor and calibration factor proposed by Krueger et al. (2012) while calibration factor proposed by Ballestrin et al. (2004) underestimates the incident flux [12,15]. The calculated heat flux is also in good agreement with literature when heat flux gage moves ~30 mm away from the focal point while in between proposed calibration method overestimates the incident flux. In authors' point of view, this variation is due to non-uniform temperature distribution on the Lambertian target which results in biasing the calculations. The temperature at the 'Thermocouple inner right' shown in Figure 4 becomes higher as it is moved towards the focal point while other thermocouples do not show that much variation. Average temperature obtained from these thermocouples was used to calculate energy absorbed by the Lambertian target per Equation 4. It was observed that the average temperature was lower than the temperature obtained from the 'thermocouple inner right' thereby underestimating the energy absorbed by the Lambertian target. This underestimation in energy absorption results in the overestimation of energy absorbed by the heat flux gage. Further system improvements are required to maintain uniform temperature on the Lambertian target to obtain unbiased results. This can be achieved either by designing heat exchanger capable of maintaining uniform temperature of the Lambertian target or by restricting incident flux on to the heat flux gage only.

Flux distribution of the 7 kW solar simulator can be adopted to a typical daily cycle of direct normal radiation as measured by the National Renewable Energy Laboratory (NREL) database at location 39.472˚ North and 105.18˚ West [27]. For example, data for direct solar irradiance measured on May 28th, 2014 by NREL is given in Figure 7. It can be observed that the peak flux is reached at the time of the highest solar zenith angle while flux levels decrease before and after midday. Because of tracking the sun, flux levels show more uniform distribution throughout the day compared to direct irradiance along horizontal flat surface.

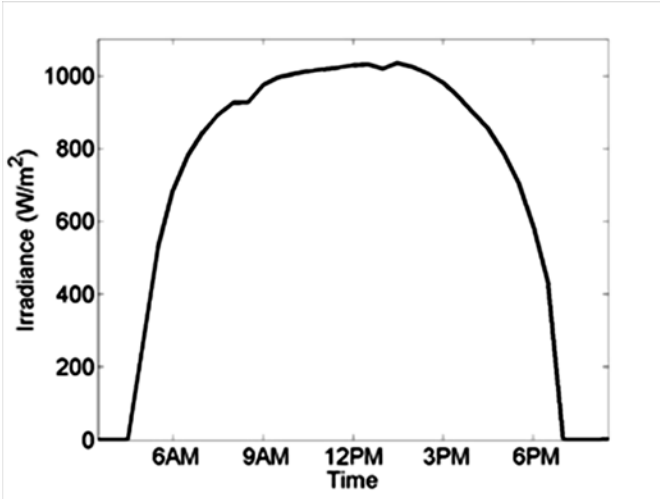

Figure 7 Direct solar irradiance measured by NREL in May 28th, 2014

A dimensionless distribution, *X(t)*, of incoming direct solar radiation I_{direct} (as in Figure 7) throughout the day can be used as reference to calculate the percent rate of radiation flux per NREL measurement at selected times of the day *t* in terms of the maximum measured flux of the day:

$$X(t) = \frac{I_{NREL}(t)}{I_{NREL,max}} \tag{8}$$

Dimensionless intraday variation was imprinted on flux distribution measurements of the solar simulator by fitting to a Gaussian function $f\,(r)$ using Matlab. In order to obtain an analytical description of $flux(t,r)$ for the measured profile at each corresponding time of the day, the following equation was used:

$$flux(t,r) = percentage(t)\, f(r) \tag{9}$$

The distribution function $flux(t,r)$ gives an adjusted solar simulator flux profile adapted to time dependent actual NREL measurements throughout a day. Figure 8 shows corresponding simulator peak heat fluxes derived from the NREL data in conjunction with the 7 kW solar simulator measurements. Correspondent solar simulator flux profile at each time of the day was used to analytically derive optimal aperture size in order to maintain constant heat flux and temperature inside the

reactor. Two different solutions were implemented based on calculations made by Steinfeld (1993) and first order heat transfer analysis [1]. Air was used as the medium and it was assumed non-participating.

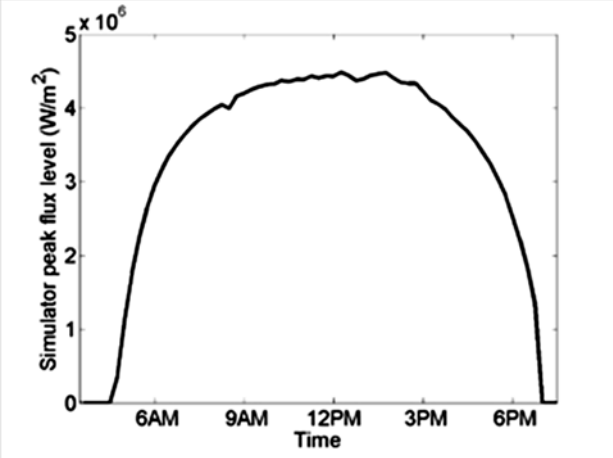

Figure 8 Adapted solar simulator peak flux levels to simulate different times of the day

As stated in Steinfeld (1993), optimal temperature and radius of aperture depend on the peak heat flux [1]. Thus, Steinfeld's formulations were used to calculate the optimal reactor temperature and radius at each time of the day as presented in Figure 9. Maximal optimal temperature for corresponding midday at simulator peak flux of 450 W/cm^2 was calculated as 1133 K, which was in good agreement with the optimum temperature of 1147 K for a peak heat flux of 456 W/cm^2 as derived in Steinfeld (1993) [1]. In order to achieve appreciable high temperature inside the reactor, concentrated solar radiation can be used starting at 5 am (MST) when the peak heat flux is $1.13x10^6\ W/m^2$, which results in an optimal temperature T_0 of 891 K at an aperture radius of 3.52 cm. Intercepted heat flux at the aperture for optimal temperature and radius at 5 am (MST) was calculated from

$$q_{absorption}(t, r_0) = \alpha_{eff} \int_0^{r_0} 2\,\pi\, r\, flux\,(t,r)\, dr \tag{10}$$

and re-radiation was computed from

$$q_{rerad}(r_0) = \varepsilon_{eff}\, \sigma\, T^4\, \pi\, r_0^2 \tag{11}$$

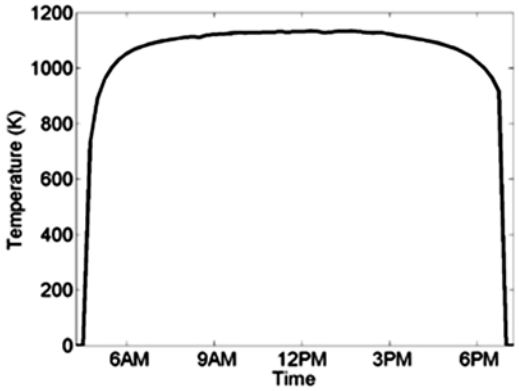

Figure 9 Optimal temperature as function of peak heat fluxes only as in Steinfeld (1993) [1]

Effective absorptivity of $\alpha_{eff} = 0.96$ and effective emissivity of $\varepsilon_{eff} = 0.96$ were used in calculations. Difference between the absorbed and re-radiated flux gives the net radiative heat flux to the reactor. The net heat flux from the starting point of t_0 = 5 am (MST) is equal to q_{net} = 533 W. In order to maintain that constant temperature and the net heat flux; the aperture size has to be adjusted during the day by solving Equation 12 for r per $q_{net}(t) = q_{net}(t_0) = const$ and $T = T_0$ as follows

$$q_{net}(t) = q_{absorption}(t, r) - q_{rerad}(T, r) \tag{12}$$

Control volume analysis of the reactor gives the following

$$q_{net}(t) = q_{fluid} = (T - T_{in})\, c_p\, \dot{m}_{gas} \tag{13}$$

which yields that the flow rate of the gas should be in the range of 36.38 slpm to reach this temperature. It is hereby assumed that the outlet temperature of the fluid equals the wall temperature and conduction losses through the reactor walls are neglected. However, it should be noted that 36.38 slpm feedstock flow rate at this temperature may reduce chemical conversion rate because of reducing the residence time. Thus, findings imply that theoretically found optimal values of aperture radius and reactor temperature are technically not favourable. A reduced flow rate, for example, 10 slpm, would yield higher residence time and therefore higher conversion efficiency. The combination of Equations 10 to 13 leads to an implicit formulation of aperture radius and reactor temperature as follows

$$\alpha_{eff} \int_0^{r_0} 2\pi r\, flux(t,r)\, dr = \varepsilon_{eff}\, \sigma\, T^4\, \pi\, r_0^2 + (T - T_{in}) c_p \dot{m}_{gas} \tag{14}$$

Wall and gas outlet temperatures were calculated using Equation 14. Optimal radius was then determined by the highest gas outlet temperature at specific time of the day. Results showed that in order to reach a gas outlet temperature of 1339 K at the given flow rate, the optimal aperture size at 5 am should be 1.8 cm as seen in Figure 11. To keep the temperature constant, aperture radius has to be adapted during daytime as described per Equation 12 and as seen in Figure 12.

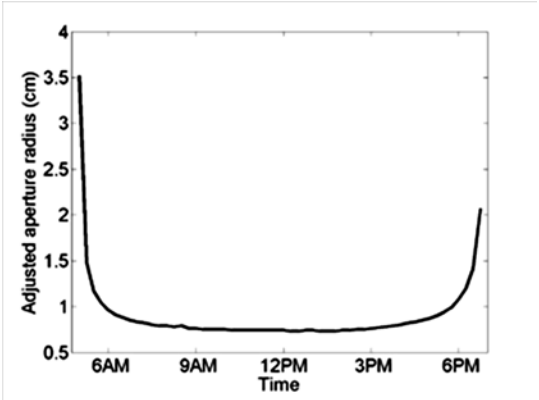

Figure 10 Variable aperture radii to maintain constant temperature of 891 K and net heat flux of 533 W from 5am to 6:45pm

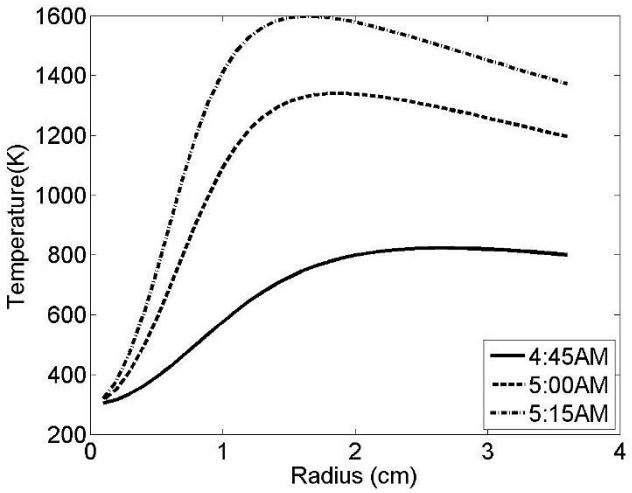

Figure 11 Steady temperatures at different radii for selected times of the day and constant flow rate of 10 slpm

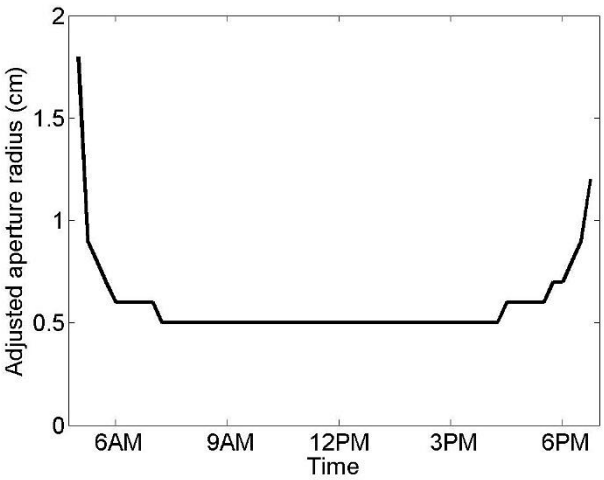

Figure 12 Variable aperture radii to maintain temperature of 1339 K from 5 am to 6:45 pm per net heat flux of 257 W

For comparison, it is seen that the temperatures obtained by Ballestrin et al. (2004) are lower whereas maximal temperature at 5 am and 4:45 am drops to 854 K and 533 K, respectively. Corresponding adjusted aperture sizes change to a radius of 2.5 cm during sunset and smaller ones of 0.4 cm during midday, which is caused by the different shape of the measured flux distribution.

Effective absorptivity and emissivity used in optimization were calculated by TracePRO ray tracing simulations for a given reactor geometry described in Costandy et al. (2012) [28]. Inner reactor walls were modelled as surface sources at the reactor temperature. Effective emissivity was calculated as follows:

$$\varepsilon_{eff} = \frac{q_{out}}{\sigma T^4 A_{Aperture}} \quad (15)$$

The results showed that for the given reactor design, effective emissivity decreased only by 0.73% when the aperture radius was increased from 1 to 4 cm. This implies that emissivity of ε = 0.96 can be modelled independent of the radius. The results further imply that the effective absorptivity does not significantly differ from emissivity either, e.g. 0.8% at a radius of 4 cm. This leads to the assumption that the effective absorptivity is equal to effective emissivity and therefore performed emissivity calculations can be used for absorptivity as well. It should be noted that, if an inner absorptivity of 0.4 is assumed, slightly lower values of effective absorptivity such as 0.91 are obtained which supports the assumption of radius-independency.

CONCLUSION

Radiation distribution of a high flux solar simulator was presented. In calculations, a uniform flux distribution was assumed whereas a non-uniform flux was incident on the system during the experiments. This assumption underestimates the energy being absorbed by the Lambertian target which consequently overestimates the energy absorbed by the heat flux gage. This can be avoided by assuming variable incident heat flux on the system and quantifying the radiation distribution of the solar simulator along with maintaining uniform temperature of the Lambertian target either by designing heat exchanger or restricting incident flux on to the heat flux gage only.

Flux profiles found by experiments were used in identifying optimum aperture sizes for different flux levels mimicking solar power behaviour from sunrise to sunset. It was found that reactor temperature of 1339 K can be maintained by changing corresponding intraday aperture sizes from 1.8 cm to 0.5 cm. Results imply that this method may overestimate reactor temperature, especially at lower peak fluxes.

REFERENCES

[1] Steinfeld, A. and Schubnell, M., Optimum aperture size and operating temperature of a solar cavity receiver. Solar Energy, 1993. 50(1): p. 19-25.
[2] Usman, S. and Ozalp, N., Numerical and optical analysis of solar power level adaptable solar reactor. Heat Transfer Engineering, 2014. 35(16-17): p.1405-1417.
[3] Kuhn, P. and Hunt, A., A new solar simulator to study high temperature solid-state reactions with highly concentrated radiation. Solar Energy Materials, 1991. 24(1-4): p. 742-750.
[4] Gordon, J.M., Babai, D., and Feuermann, D., A high-irradiance solar furnace for photovoltaic characterization and nanomaterial synthesis. Solar Energy Materials and Solar Cells, 2011. 95(3): p. 951-956.
[5] Gevorgyan, S.A., Carlé, J.E., Søndergaard, R., Larsen-Olsen, T.T., Jørgensen, M. and Krebs, F.C., Accurate

characterization of OPVs: Device masking and different solar simulators. Solar Energy Materials and Solar Cells, 2013. 110(0): p 24-35.
[6] Lewandowski, A., Bingham, C., O'Gallagher, J., Winston, R. and Sagie, D., Performance characterization of the SERI high-flux solar furnace. Solar Energy Materials, 1991. 24(1-4): p. 550-563.
[7] Neumann, A. and Groer, U., Experimenting with concentrated sunlight using the DLR solar furnace. Solar Energy, 1996. 58(4–6): p. 181-190.
[8] Hirsch, D., v. Zedtwitz, P., Osinga, T., Kinamore, J. and Steinfeld, A., A new 75 kW high-flux solar simulator for high-temperature thermal and thermochemical research. Journal of Solar Energy Engineering, 2003. 125(1): p. 117-120.
[9] Petrasch, J., Coray, P., Meier, A., Brack, M., Haeberling, P., Wuillemin, D. and Steinfeld, A., A novel 50 kW 11,000 suns high-flux solar simulator based on an array of xenon arc lamps. Journal of Solar Energy Engineering, 2006. 129(4): p. 405-411.
[10] Guesdon, C., Alxneit, I., Tschudi, H.R., Wuillemin, D., Petrasch, J., Brunner, Y., Winkel, L. and Sturzenegger, M., PSI's 1 kW imaging furnace—A tool for high-temperature chemical reactivity studies. Solar Energy, 2006. 80(10): p. 1344-1348.
[11] Llorente, J., Ballestrín, J., and Vázquez, A.J., A new solar concentrating system: Description, characterization and applications. Solar Energy, 2011. 85(5): p. 1000-1006.
[12] Krueger, K.R., Lipiński, W, and Davidson, J.H., Operational performance of the University of Minnesota 45 kW_e high-flux solar simulator. ASME 6th International Conference on Energy Sustainability & 10th Fuel Cell Science, Engineering and Technology Conference, 2012. San Diego, CA.
[13] Lee, H., Chai, K., Kim, J., Lee, S., Yoon, H., Yu, C. and Kang, Y., Optical performance evaluation of a solar furnace by measuring the highly concentrated solar flux. Energy, 2013(0).
[14] Sequoia. Vatell calibrations. Retrieved in February 2015 from http://www.sequoia.co.uk/product.php?id=200#Downloads.
[15] Ballestrín, J. and Monterreal, R., Hybrid heat flux measurement system for solar central receiver evaluation. Energy, 2004. 29(5–6): p. 915-924.
[16] Jackson, R.L., Bhavnani, S.H., and Ferguson, T.P., A Multiscale model of thermal contact resistance between rough surfaces. Journal of Heat Transfer, 2008. 130(8): p. 081301-081301.
[17] Song, S. and Yovanovich, M.M., Relative contact pressure: Dependence on surface roughness and vickers microhardness. International Journal of Thermophysics, 1988. 2(1): p. 43-47.
[18] Yovanovich, M.M., Four decades of research on thermal contact, gap, and joint resistance in microelectronics. IEEE Transactions on Components and Packaging Technologies, 2005. 28(2): p. 182-206.
[19] Sarwar, J., Georgakis, G, LaChance, R. and Ozalp, N., Description and characterization of an adjustable flux solar simulator for solar thermal, thermochemical and photovoltaic applications. Solar Energy, 2014. 100(0): p. 179-194
[20] Osram product data sheet for OSRAM. XBO 7000 W/HS CL OFR. Retrieved in June 2013 from http://www.osram.com/osram_com/products/lamps/specialty-lamps/xbo/xbo-classic-line/index.jsp.
[21] Shimokawa, R., Takahashi, T., Takato, H., Ozaki, A. and Takano, Y., 2μm thin film c-Si cells on near-Lambertian Al2O3 substrates. Solar Energy Materials and Solar Cells, 2001. 65(1–4): p. 593-598.
[22] National Instruments. C. NI 9213: 16-channel thermocouple input module. Retrieved in February 2015 from http://sine.ni.com/nips/cds/print/p/lang/en/nid/208788.
[23] National Instruments. C. NI 9211: 4-Channel, 14 S/s, 24-Bit, ±80 mV Thermocouple Input Module. Retrieved in February 2015 from http://sine.ni.com/nips/cds/view/p/lang/en/nid/208787.
[24] Vatell, Certificate of Calibration, in Vatell Corporation2012. p. 1.
[25] Newmark Systems. I. NLS8 linear stage. Retrieved in February 2015 from http://www.newmarksystems.com/linear-positioners/nls8-series-linear-stage/.
[26] Newmark Systems. I. NSC-G series motion controller. Retrieved in February 2015 from http://www.newmarksystems.com/motion-controllers/nsc-g-series/.
[27] NREL Database. Daily Plots and Raw Data Files, Direct CH1 for 5/28/2014. Retrieved in February 2015 from http://www.nrel.gov/midc/srrl_bms/.
[28] Constandy, J., El Ghazal, N., Mohamed, M.T., Menon, A., Shilapuram, V. and Ozalp, N., Effect of reactor geometry on the temperature distribution of hydrogen producing solar reactors. International Journal of Hydrogen Energy, 2012. 37(21): p. 16581-16590.